Comput Mech (2015) 55:1211–1225
DOI 10.1007/s00466-015-1166-x

Dynamic and fluid–structure interaction simulations of bioprosthetic heart valves using parametric design with T-splines and Fung-type material models

Ming-Chen Hsu[1] · David Kamensky[2] · Fei Xu[1] · Josef Kiendl[3] · Chenglong Wang[1] · Michael C. H. Wu[1] · Joshua Mineroff[1] · Alessandro Reali[3] · Yuri Bazilevs[4] · Michael S. Sacks[2]

Received: 21 April 2015 / Accepted: 2 May 2015 / Published online: 26 May 2015

Abstract This paper builds on a recently developed immersogeometric fluid–structure interaction (FSI) methodology for bioprosthetic heart valve (BHV) modeling and simulation. It enhances the proposed framework in the areas of geometry design and constitutive modeling. With these enhancements, BHV FSI simulations may be performed with greater levels of automation, robustness and physical realism. In addition, the paper presents a comparison between FSI analysis and standalone structural dynamics simulation driven by prescribed transvalvular pressure, the latter being a more common modeling choice for this class of problems. The FSI computation achieved better physiological realism in predicting the valve leaflet deformation than its standalone structural dynamics counterpart.

Keywords Fluid–structure interaction · Bioprosthetic heart valve · Isogeometric analysis · Immersogeometric analysis · Arbitrary Lagrangian–Eulerian · NURBS and T-splines · Kirchhoff–Love shell · Fung-type hyperelastic model

✉ Ming-Chen Hsu
jmchsu@iastate.edu

[1] Department of Mechanical Engineering, Iowa State University, 2025 Black Engineering, Ames, IA 50011, USA

[2] Center for Cardiovascular Simulation, Institute for Computational Engineering and Sciences, The University of Texas at Austin, 201 East 24th St, Stop C0200, Austin TX 78712, USA

[3] Department of Civil Engineering and Architecture, University of Pavia, via Ferrata 3, 27100 Pavia, Italy

[4] Department of Structural Engineering, University of California, San Diego, 9500 Gilman Drive, Mail Code 0085, La Jolla, CA 92093, USA

1 Introduction

Heart valves serve to ensure unidirectional flow of blood through the circulatory systems of humans and many animals. Heart valves consist of thin, flexible leaflets that open and close passively, in response to blood flow and the movements of the attached cardiac structures. Primarily in aortic heart valves, the leaflets may become diseased and, in some cases, valves must be replaced by prostheses. Hundreds of thousands of such devices are implanted in patients every year [1,2].

The most popular class of prostheses are bioprosthetic heart valves (BHVs). BHVs imitate the structure of the native valves, consisting of flexible leaflets fabricated from chemically-treated soft tissues. BHVs do not induce blood damage that can occur due to prostheses composed of rigid mechanical parts [2–4]. However, BHVs are less durable than their mechanical counterparts and require replacement, typically after 10–15 years, due to calcification and structural damage [5]. In spite of this long-standing problem, BHV material technologies have not changed since their introduction more than 30 years ago.

Improved durability remains an important clinical goal and represents a unique cardiovascular engineering challenge, resulting from the extreme valvular mechanical demands. Yet, current BHV assessment relies exclusively on device-level evaluations, which are confounded by simultaneous and highly coupled biomaterial mechanical fatigue, valve design, hemodynamics, and calcification. Thus, despite decades of clinical BHV usage and growing popularity, there exists no acceptable method for simulating BHV durability in any design context. There is thus a profound need for the development of novel simulation technologies that combine state-of-the-art fluid–structure interaction (FSI) analysis with novel constitutive models of BHV bio-

material responses, to simulate long-term cyclic loading [6,7].

Computational modeling of continuum mechanics has proven tremendously beneficial to the design process of many other products, but BHVs present unique challenges for computational analysis, and cannot yet be conveniently simulated using "off-the-shelf" software. The effect of hydrostatic forcing on a closed BHV may be modeled as a prescribed pressure load and simulated using standard FEM (see, e.g., [8–10]), but such models cannot capture the transient response of an opening valve or the so-called "water hammer effect" in a closing valve. Both of these phenomena likely contribute to long-term structural fatigue, but neither can be modeled without accounting for the surrounding hemodynamics. A complete mechanical model of a BHV must therefore include FSI.

In [11,12], we developed a new numerical method that, in the tradition of immersed boundary methods [13–16], allows the structure discretization to move independently of the background fluid mesh. In particular, we focused on directly capturing design geometries in the unfitted analysis mesh and identified our technique with the concept of *immersogeometric analysis*. The methods that we developed in [11,12] made beneficial use of isogeometric analysis (IGA) [17,18] to discretize both the structural and fluid mechanics subproblems involved in the FSI analysis of BHVs. In this paper, we further advance our immersogeometric FSI methodology for BHVs by focusing on automating the IGA model design and improving constitutive modeling of the chemically-treated tissues forming the BHV leaflets.

Despite recent progress, several challenges remain in the effective use of IGA to improve the engineering design process. A major difficulty toward this end remains automatic (or semi-automatic) construction of analysis-suitable IGA models. In many cases, intimate familiarity with computer-aided design (CAD) technology and advanced programming skills are required to create high-quality IGA geometries and meshes. In a recent work [19] the authors introduced an interactive geometry modeling and parametric design platform that streamlines the engineering design process by hiding the complex CAD functions in the background through generative algorithms, and letting the user control the design through key parameters. In the present work, we apply this design-through-analysis framework to BHV analysis.

We further enhance the realism of the BHV FSI by extending the isogeometric rotation-free Kirchhoff–Love thin shell formulation [20,21] used in the prior work to include the soft-tissue constitutive modeling framework developed in [22]. An important feature of the framework in [22] is that it can accommodate arbitrary hyperelastic constitutive models, which adds a great deal of flexibility to the BHV FSI methodology developed in this work.

The remainder of this paper is structured as follows. Section 2 describes our BHV FSI modeling framework and methods. In Sect. 3, we construct a discrete model of a BHV immersed in the lumen of a flexible artery and apply the methodology of Sect. 2 to perform a BHV FSI simulation. We compare the FSI results with the results of a standalone structural dynamics BHV simulation driven by prescribed transvalvular pressure, considered to be "state-of-the-art" in the biomechanics community [9]. Section 4 draws conclusions.

2 BHV FSI modeling framework and methods

In this section we present the main constituents of the recently developed FSI modeling framework for heart valves, focusing on the novel contribution of the present article. We begin by providing a discussion of the recently developed parametric design-through-analysis platform for IGA [19] and its use in the modeling of heart valve geometry. We then summarize the shell formulation proposed in [22], which we use to incorporate incompressible Fung-type hyperelastic material behavior into our BHV simulations. We then provide an overview of the immersogeometric FSI [11] procedures employed to simulate this challenging class of problems.

2.1 Parametric modeling of heart valve geometry

In [19], an interactive geometry modeling and parametric design platform was proposed to help design engineers and analysts make effective use of IGA. Several Rhinoceros (Rhino) [23] "plug-ins", with a user-friendly interface, were created to take input design parameters, generate parameterized surface and/or volumetric models, perform computations, and visualize the solution fields, all within the same CAD program. An important aspect of the proposed platform is the use of generative algorithms for IGA model creation and visualization. In this work, we make use of the developed platform to automate the geometry design of BHV models for use in FSI analysis.

The developments in [19] were based on Rhino CAD software, which gives designers a variety of functions that are required to build complex, multi-patch NURBS surfaces [25]. Recently, additional functionality was added in Rhino to create and manipulate T-spline surfaces [24,26]. This is an important enhancement that allows one to move away from a fairly restrictive NURBS-patch-based geometry design to a completely unstructured, watertight surface definition respecting all the constraints imposed by analysis [27,28]. Rhino also features a graphic programming interface called Grasshopper [29] suitable for parametric design, and utilizes open-source software development kits (SDK) [30] for plug-in development. Furthermore, Rhino is relatively transparent as compared to other CAD software in that it provides the user with the ability to interact with the

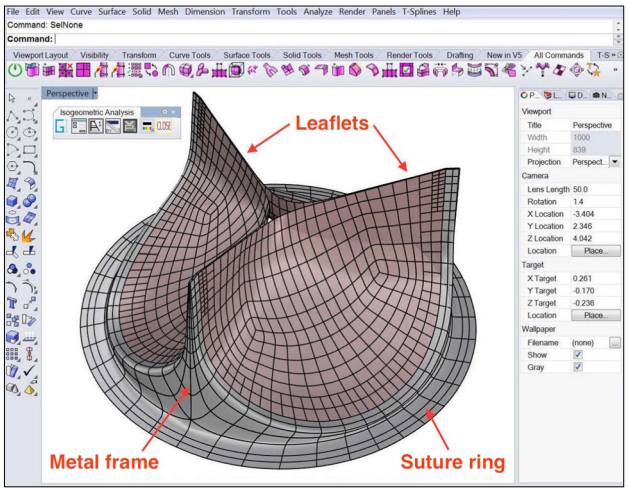

Fig. 1 The trileaflet T-spline BHV model in Rhino. The T-spline surfaces were generated using the in-house parametric modeling platform (see Fig. 2) and the Autodesk T-Splines Plug-in for Rhino [24]

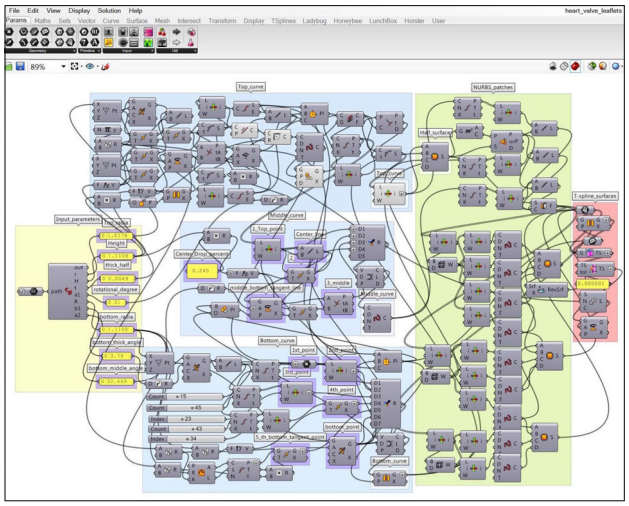

Fig. 2 The Grasshopper program for parametric BHV leaflet geometry modeling. The major geometry construction steps are shown in Fig. 3

system through the plug-in commands. All of these features are well aligned with the needs of analysis-suitable geometry design for BHVs, and are employed in the present work.

Figure 1 shows a snapshot of the Rhino CAD modeling software interface, with the T-spline BHV model used in the computations of the present paper. This BHV leaflet geometry is based on a 23-mm design by Edwards Lifesciences [8, 31]. The NURBS version of this model was analyzed earlier in [11,12]. In the present case, the leaflets of the BHV are modeled using three cubic T-spline surfaces, as shown in Fig. 1. The use of unstructured T-splines enables local refinement and coarsening [32] and avoids the small, degenerated NURBS elements near the commissure points used in [11, 12]. To improve the realism of the simulation, we include the metal stent in the BHV model. Although this complicates the geometry, it presents no difficulty for the design platform employed in this work to generate a single watertight surface.

Using Grasshopper as a visual programming tool, the program that creates an analysis-suitable geometry design is written in terms of "components" with pre-defined or user-defined functionalities, and "wire connections" between the components that serve as conduits of input and output data. As a result, using an intuitive arrangement of components and connections one can rapidly generate an analysis model and establish parametric control over the design. A Grasshopper program for the geometry design of the BHV leaflet employed in this work is shown in Fig. 2. The visual program executes the following geometry construction steps (see Fig. 3 for a visual illustration): Parametric input is used to construct NURBS curves, which are the bounding curves for the NURBS surface patches that define the valve leaflet geometry. The resulting multi-patch NURBS geometry is then re-parameterized to create a single T-spline surface geometry. Following this workflow, new analysis-suitable geometries can be easily and efficiently generated using different sets of input design parameters.

Remark 1 Note that the stent can be generated using the same parametric geometry modeling approach. It is not included in Figs. 2 and 3 for the sake of clarity and simplicity of presentation.

2.2 Shell structural formulation

The leaflet structure is modeled as a hyperelastic thin shell with isogeometric discretization as presented in Kiendl et al. [22]. Due to the Kirchhoff–Love hypothesis of normal cross sections, a point $\mathbf{x}$ in the shell continuum can be described by a point $\mathbf{r}$ on the midsurface and a normal vector $\mathbf{a}_3$ to the midsurface as

$$\mathbf{x}\left(\xi^1,\xi^2,\xi^3\right)=\mathbf{r}\left(\xi^1,\xi^2\right)+\xi^3\,\mathbf{a}_3\left(\xi^1,\xi^2\right), \tag{1}$$

where ξ^1,ξ^2 are the surface coordinates, $\xi^3\in[-h_{\text{th}}/2,h_{\text{th}}/2]$ is the thickness coordinate, and h_{th} is the shell thickness. Covariant base vectors and metric coefficients are defined by $\mathbf{g}_i=\mathbf{x}_{,i}$ and $g_{ij}=\mathbf{g}_i\cdot\mathbf{g}_j$, respectively, where the notation $(\cdot)_{,i}=\partial(\cdot)/\partial\xi^i$ is used for partial derivatives. Furthermore, we adopt the convention that Latin indices take on values $\{1,2,3\}$ while Greek indices take on values $\{1,2\}$. Contravariant base vectors $\mathbf{g}^i$ are defined by the Kronecker delta property $\mathbf{g}^i\cdot\mathbf{g}_j=\delta^i_j$ and contravariant metric coefficients can be obtained by the inverse matrix $[g^{ij}]=[g_{ij}]^{-1}$.

For the shell model, only in-plane components of g_{ij} are considered and terms that appear quadratic in ξ^3 are neglected, such that

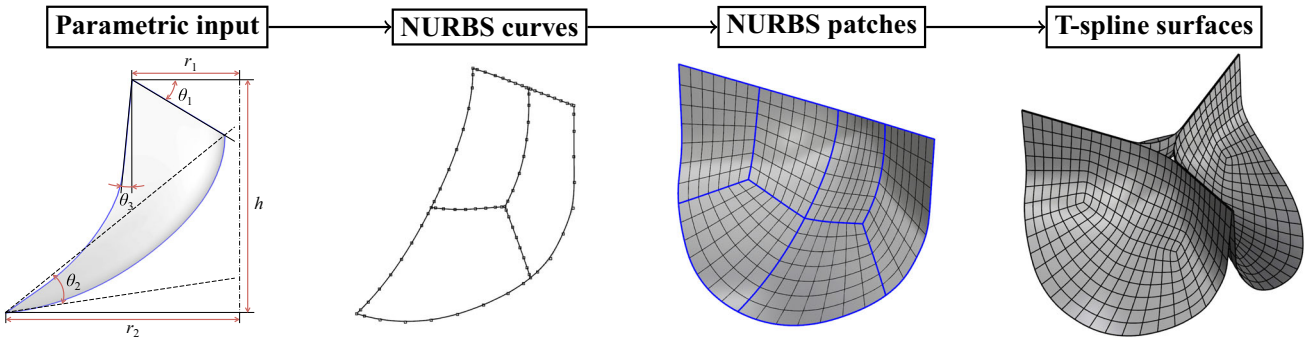

Fig. 3 Parametric BHV leaflet geometry modeling flowchart

$$g_{\alpha\beta} = a_{\alpha\beta} - 2\,\xi^3 b_{\alpha\beta}. \tag{2}$$

In the above, $a_{\alpha\beta}$ and $b_{\alpha\beta}$ are the first and second fundamental form of the midsurface, respectively, obtained as $a_{\alpha\beta} = \mathbf{a}_\alpha \cdot \mathbf{a}_\beta$ and $b_{\alpha\beta} = \mathbf{a}_{\alpha,\beta} \cdot \mathbf{a}_3$, where

$$\mathbf{a}_\alpha = \mathbf{r}_{,\alpha}, \tag{3}$$

$$\mathbf{a}_3 = \frac{\mathbf{a}_1 \times \mathbf{a}_2}{||\mathbf{a}_1 \times \mathbf{a}_2||}, \tag{4}$$

are the tangent base vectors and unit normal vector of the midsurface, respectively.

The above equations are valid for both deformed and undeformed configurations, where variables of the latter will be indicated by a symbol $\mathring{(\cdot)}$, for example, $\mathring{\mathbf{x}}$, $\mathring{\mathbf{g}}_{,i}$, $\mathring{g}_{ij}$, etc. The Jacobian determinant of the mapping from the undeformed to the deformed configuration is given by

$$J = \sqrt{|g_{ij}|/|\mathring{g}_{ij}|}. \tag{5}$$

Furthermore, we introduce the in-plane Jacobian determinant J_o as

$$J_o = \sqrt{|g_{\alpha\beta}|/|\mathring{g}_{\alpha\beta}|}. \tag{6}$$

The weak form of the shell structural formulation is stated as follows:

$$\int_{\Gamma_t} \mathbf{w} \cdot \rho h_{\text{th}} \left.\frac{\partial^2 \mathbf{y}}{\partial t^2}\right|_{\mathbf{X}} \mathrm{d}\Gamma + \int_{\Gamma_0}\int_{h_{\text{th}}} \delta\mathbf{E} : \mathbf{S}\,\mathrm{d}\xi^3 \mathrm{d}\Gamma - \int_{\Gamma_t} \mathbf{w} \cdot \rho h_{\text{th}} \mathbf{f}\,\mathrm{d}\Gamma - \int_{\Gamma_t} \mathbf{w} \cdot \mathbf{h}^{\text{net}}\,\mathrm{d}\Gamma = 0, \tag{7}$$

where $\mathbf{y}$ is the displacement of the shell midsurface, $\partial(\cdot)/\partial t|_{\mathbf{X}}$ is the time derivative holding the material coordinates $\mathbf{X}$ fixed, ρ is the density, $\mathbf{S}$ is the second Piola–Kirchhoff stress, $\delta\mathbf{E}$ is the variation of the Green–Lagrange strain corresponding to a displacement variation $\mathbf{w}$, $\mathbf{f}$ is a prescribed body force, $\mathbf{h}^{\text{net}} = \mathbf{h}(\xi^3 = -h_{\text{th}}/2) + \mathbf{h}(\xi^3 = h_{\text{th}}/2)$ is the total traction contribution from the two sides of the shell, and Γ_0 and Γ_t are the shell midsurface in the reference and deformed configurations, respectively. The Green–Lagrange strain is defined as

$$\mathbf{E} = \frac{1}{2}(\mathbf{C} - \mathbf{I}), \tag{8}$$

where $\mathbf{C}$ is the left Cauchy–Green deformation tensor and $\mathbf{I}$ the identity tensor. Only in-plane strains are computed, which are obtained as

$$E_{\alpha\beta} = \frac{1}{2}(g_{\alpha\beta} - \mathring{g}_{\alpha\beta}). \tag{9}$$

The second Piola–Kirchhoff stress is obtained from a hyperelastic strain-energy density function ψ as

$$\mathbf{S} = \frac{\partial\psi}{\partial\mathbf{E}} = 2\frac{\partial\psi}{\partial\mathbf{C}}. \tag{10}$$

Linearizing Eq. (10), we obtain the tangent material tensor

$$\mathbb{C} = \frac{\partial\mathbf{S}}{\partial\mathbf{E}} = 4\frac{\partial^2\psi}{\partial\mathbf{C}^2}. \tag{11}$$

In this paper, we assume an incompressible material, where the elastic strain energy function ψ_{el} is classically augmented by a constraint term enforcing incompressibility, i.e., $J = 1$, via a Lagrange multiplier p, which can be identified as the hydrostatic pressure [33]:

$$\psi = \psi_{el} - p(J - 1). \tag{12}$$

For shell analysis, we can use the plane stress condition, $S^{33} = 0$, in order to analytically determine and eliminate the Lagrangian multiplier p. Furthermore, we eliminate the transverse normal strains E_{33} from the equations by static condensation of the tangent material tensor. The detailed derivations can be found in [22]. Eventually, we obtain the

following equations for the shell's stress and material tangent tensors:

$$S^{\alpha\beta} = 2\frac{\partial \psi_{el}}{\partial C_{\alpha\beta}} - 2\frac{\partial \psi_{el}}{\partial C_{33}} J_o^{-2} g^{\alpha\beta}, \tag{13}$$

$$\begin{aligned}\mathbb{C}^{\alpha\beta\gamma\delta} = {} & 4\frac{\partial^2 \psi_{el}}{\partial C_{\alpha\beta}\partial C_{\gamma\delta}} + 4\frac{\partial^2 \psi_{el}}{\partial C_{33}^2} J_o^{-4} g^{\alpha\beta} g^{\gamma\delta} \\ & - 4\frac{\partial^2 \psi_{el}}{\partial C_{33}\partial C_{\alpha\beta}} J_o^{-2} g^{\gamma\delta} - 4\frac{\partial^2 \psi_{el}}{\partial C_{33}\partial C_{\gamma\delta}} J_o^{-2} g^{\alpha\beta} \\ & + 2\frac{\partial \psi_{el}}{\partial C_{33}} J_o^{-2} \left(2g^{\alpha\beta} g^{\gamma\delta} + g^{\alpha\gamma} g^{\beta\delta} + g^{\alpha\delta} g^{\beta\gamma}\right).\end{aligned} \tag{14}$$

With Eqs. (13) and (14), arbitrary 3D constitutive models can be used for shell analysis directly. Given the first and second derivatives of the elastic strain energy function, the incompressibility and plane stress constraints, as well as static condensation of the thickness stretch, are all included by the additional terms in Eqs. (13) and (14). Recalling Eq. (2), it can be seen that the whole formulation can be completely described in terms of the first and second fundamental forms of the shell midsurface, and using only displacement degrees of freedom.

To discretize the shell equations we use IGA based on T-splines, which have the necessary continuity properties. The details of constructing smooth T-spline basis functions can be hidden from the analysis code through the use of Bézier extraction [34]. The extraction operators specifying the relationship between the T-spline basis functions and Bernstein polynomial basis on each Bézier element can be generated automatically by the Autodesk T-Splines Plug-in for Rhino [24,26]. The mesh of Bézier elements for our T-spline BHV model is shown in Fig. 4.

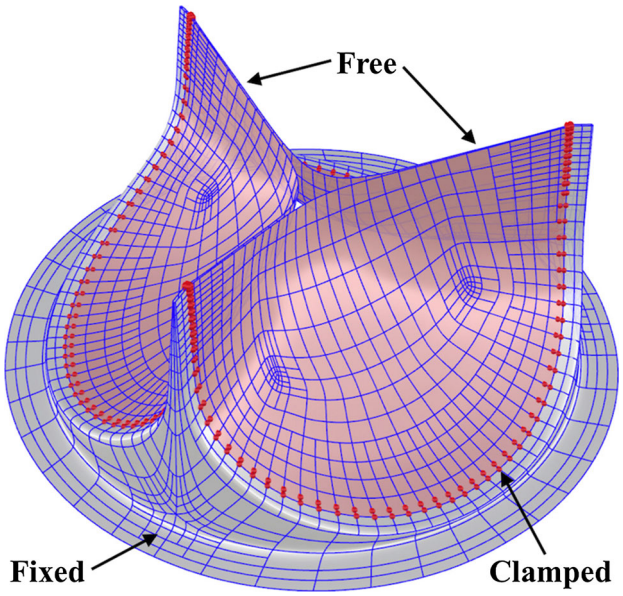

Fig. 4 The Bézier elements defining the T-spline surface used in the shell analysis. The clamped boundary condition is applied to the leaflet attachment edge by fixing two rows of T-spline control points highlighted in the figure. (The *points* in the second row away from the edge are also called tangency handles)

2.3 Immersogeometric FSI

In this section we summarize the main constituents of our framework for immersogeometric FSI, as it applies to the simulation of BHVs. For mathematical and implementation details the reader is referred to [11,12,35]. Our immersogeometric approach to BHV FSI analysis combines the following computational technologies into a single framework:

- The blood flow in a deforming artery is governed by the Navier–Stokes equations of incompressible flows posed on a moving domain. The domain motion is handled using the Arbitrary Lagrangian–Eulerian (ALE) formulation [36,37], which is a widely used approach for vascular blood flow applications [38–44]. For an overview of the ALE method in cardiovascular fluid mechanics, see [45,46]. These two references also include an overview of the space–time approach to moving domains [47–51], which has also been applied to a good number of cardiovascular fluid mechanics computations, with the most recent ones reported in [52–55].
- The blood flow domain follows the motion of the deformable artery wall, which is governed by equations of large-deformation elastodynamics written in the Lagrangian frame [56]. In the present work, the discretization between blood flow and artery wall is assumed to be conforming, and is handled using a monolithic FSI formulation described in detail in [57].
- The discretization of the Navier–Stokes equations makes use of a combination of NURBS-based IGA and ALE–VMS [58–60]. The ALE–VMS formulation may be interpreted both as a stabilized method [47,61,62] and as a large-eddy simulation (LES) turbulence model [47,61–67]. The discretization of the solid arterial wall also makes use of trivariate NURBS-based IGA.
- BHV leaflets are modeled as rotation-free hyperelastic Kirchhoff–Love shell structures (see [22] and the previous section) and discretized using T-splines. In the FSI framework, they are immersed into a moving blood-flow domain. The immersed FSI problem is formulated using an augmented Lagrangian approach for FSI, which was originally proposed in [68] to handle boundary-fitted mesh computations with nonmatching fluid–structure interface discretizations. It was found in [11] that the augmented Lagrangian framework naturally extends to non-boundary-fitted (i.e., immersed) FSI problems, but with

the following modifications. The tangential component of the Lagrange multiplier $\boldsymbol{\lambda}$ is formally eliminated from the formulation, resulting in weak enforcement of no-slip conditions at the fluid–structure interface [68]. The normal component of the Lagrange multiplier $\lambda = \boldsymbol{\lambda} \cdot \mathbf{n}$ is retained in the formulation in order to achieve better satisfaction of no-penetration boundary conditions at the fluid–structure interface.

- The Lagrange multiplier field is discretized by collocating the normal-direction kinematic constraint at quadrature points of the fluid–structure interface and involves adding a scalar unknown at each one of these quadrature points. In the evaluations of integrals involved in the augmented Lagrangian formulation these multiplier unknowns are treated as point values of a function defined at the fluid–structure interface. In the computations, λ is treated in a semi-implicit fashion. Namely, the penalty terms in the augmented Lagrangian formulation are treated implicitly, while the resulting penalty force is used to update λ explicitly in each time step.
- Contact between BHV leaflets is an essential feature of a functioning heart valve. During the closing stage, the BHV leaflets contact one another to prevent leakage of blood back into the left ventricle. In the context of immersed FSI approaches, pre-existing contact methods and algorithms (see, e.g., [69,70]) may be incorporated directly into the framework without any modification or concern for fluid-mechanics mesh quality. In the present work, we adopt a penalty-based approach for sliding contact and impose contact conditions at quadrature points of the shell structure. The use of smooth basis functions improves the performance of contact between valve leaflets (see, e.g., [71]).
- BHV simulations involve flow reversal at outflow boundaries, which, unless handled appropriately, often leads to divergence in the simulations. In order to preclude this backflow divergence, an outflow stabilization method originally proposed in [72] and further studied in [73] is incorporated into the FSI framework.
- We use a novel semi-implicit time integration procedure:

  1. Solve implicitly for the fluid, solid structure, mesh displacement, and shell structure unknowns, holding the Lagrange multiplier λ fixed at its current value. Note that the fluid and shell structure are coupled in this subproblem due to the presence of penalty terms in the augmented Lagrangian framework. The implicit system is formulated based on the Generalized-α technique [57,74,75].
  2. Update the Lagrange multiplier λ by adding the normal component of penalty forces coming from the fluid and structure solutions from Stage 1. In this work, we stabilize this update following reference [35], scaling the updated multiplier by $1/(1+r)$, where r is a nonnegative, dimensionless constant.

  As detailed in [11], the above semi-implicit solution procedure is algorithmically equivalent to *fully* implicit integration of a "stiff" differential-equation system approximating the constrained differential–algebraic system. The stiffness increases as the time step shrinks, but the conditioning of Stage 1 remains unaffected. A recent reference [35] showed that a stiff differential equation system is energetically stable in a simplified model problem, even when $r = 0$. To solve the nonlinear coupled problem in Stage 1, a combination of the quasi-direct and block-iterative FSI coupling strategies is adopted (see [76–79]). The complete algorithm is given in [12].

Remark 2 Our framework falls under the umbrella of the fluid–solid interface-tracking/interface-capturing technique (FSITICT) [80]. The FSITICT targets FSI problems where interfaces that are possible to track are tracked, and those too challenging to track are captured. The FSITICT was introduced as an FSI version of the mixed interface-tracking/interface-capturing technique (MITICT) [81]. The MITICT was successfully tested in 2D computations with solid circles and free surfaces [82,83], and in 3D computation of ship hydrodynamics [84]. The FSITICT was recently employed in [85] to compute several 2D FSI benchmark problems.

Remark 3 On the fluid mechanics domain interior, the mesh motion is obtained by solving a sequence of linear elastostatic problems subject to the displacement boundary conditions coming from the artery wall. In the formulation of the elastostatics problems, the Jacobian stiffening technique is employed to protect the boundary-layer mesh quality [86–89].

Remark 4 It was shown in [90–93] that imposing Dirichlet boundary conditions weakly allows the flow to slip on the solid surface, which, in turn, relaxes the boundary-layer resolution requirements to achieve the desired solution accuracy. In the non-boundary-fitted FSI, the fluid mesh is arbitrarily cut by the structural boundary, leaving a boundary-layer discretization of inferior quality compared to the boundary-fitted case. As a result, weakly enforced no-slip conditions, which naturally arise in the augmented Lagrangian framework, simultaneously lead to imposition of the physical kinematic constraints at the fluid–structure interface, and, as an added benefit, enhance the accuracy of the fluid mechanics solution near the interface.

Remark 5 During the closing stage, the BHV leaflets contact one another to block reversed flow to the left ventricle. As a result, the contact formulation employed must be such that no gap is allowed between the leaflets. This, in turn, leads to a

topology change in the problem, and presents one of the main reasons in the literature for developing non-boundary-fitted FSI techniques for the present application. Reference [53] recently demonstrated how space–time FEM, in combination with appropriately defined master–slave relationships between the mesh nodes in the fluid mechanics domain, can deliver solutions for cases with topology change without resorting to immersed techniques. The space–time with topology change (ST-TC) technique was successfully applied in the CFD simulation of an artificial heart valve with prescribed leaflet motion in [55].

3 BHV simulations

We compute pressure-driven structural dynamics and FSI of the BHV shown in Fig. 4. In particular, we consider a BHV replacing an aortic heart valve, which regulates flow between the left ventricle of the heart and the aorta. During systole, when the heart contracts, the valve permits ejection of oxygenated blood from the left ventricle into the aorta, and, during diastole, as the heart relaxes, a correctly functioning aortic valve prohibits regurgitation of blood back into the expanding ventricle. Sections 3.1 and 3.2 describe the modeling of the BHV and the surrounding artery and lumen, while Sect. 3.3 focuses on the comparison of the structural dynamics and FSI simulation results.

3.1 BHV constitutive model and boundary conditions

Biological tissues are favored in the construction of BHVs due to their unique mechanical properties. The most important of these is that they remain compliant at low strains but stiffen dramatically when stretched, allowing for ease of motion without sacrificing durability. The underlying structural mechanism is the presence of collagen fibers which are highly undulated in unloaded tissue. These fibers provide only small bending stiffnesses in unloaded tissue, but their relatively larger tensile stiffness can be recruited when they are straightened under strain. One of the earliest and most widely used models uses an exponential function of strain to describe the stiffening of tissues under tensile loading [94–96]. It is widely referred to as Fung models. For smaller bending strains, such as those in an open aortic BHV during systole, the dominant contribution to material stiffness is the extracellular matrix (ECM), which supports the network of collagen fibers. Reference [97] advocates modeling ECM as an incompressible neo-Hookean contribution to the strain-energy density functional. In this work, we combine an isotropic Fung model of collagen fiber stiffness with a neo-Hookean model of cross-linked ground matrix stiffness to obtain the following strain-energy density functional:

$$\psi_{el} = \frac{c_0}{2}\,(I_1 - 3) + \frac{c_1}{2}\left(e^{c_2(I_1-3)^2} - 1\right), \tag{15}$$

where c_0, c_1, and c_2 are material parameters. This model is combined with the incompressibility constraint as in Eq. (12). Note that while Eq. (15) is a simplified isotropic approximation to true anisotropic leaflet behaviors, it captures the important exponential nature of the BHV soft tissue behavior.

The mass density of the leaflets is set to 1.0 g/cm^3. The material parameters are set to $c_0 = 1.0 \times 10^6$ dyn/cm^2, $c_1 = 2.0 \times 10^5$ dyn/cm^2, and $c_2 = 100$. The values of c_1 and c_2 provide tensile stiffnesses that are generally comparable to those of the more complicated pericardial BHV leaflet model considered in [8]. The ECM modulus c_0 is selected to provide a small-strain bending stiffness similar to that of glutaraldehyde-treated bovine pericardium, as measured by the three-point bending tests reported in [98]. The hyperelastic thin shell analysis framework of Sect. 2.2 requires the following derivatives of the strain energy functional in Eqs. (13) and (14):

$$\frac{\partial \psi_{el}}{\partial C_{ij}} = \frac{1}{2}\left(c_0 + 2c_1c_2(I_1-3)e^{c_2(I_1-3)^2}\right)\mathring{g}^{ij}, \tag{16}$$

$$\frac{\partial^2 \psi_{el}}{\partial C_{ij}\partial C_{kl}} = c_1c_2e^{c_2(I_1-3)^2}\left(1 + 2c_2(I_1-3)^2\right)\mathring{g}^{ij}\mathring{g}^{kl}. \tag{17}$$

The BHV model employs the T-spline geometry constructed in Sect. 2.1. The T-spline mesh comprises 484 and 882 Bézier elements for each leaflet and the stent, respectively, and a total of 2301 T-spline control points. The stent is assumed rigid, and leaflet control points highlighted in Fig. 4 are restrained from moving. This clamps the attached edges of the leaflets to the rigid stent. (The stent is, for all practical purposes, rigid since it is supported by a metal frame, which is orders of magnitude stiffer than the soft tissue of the BHV leaflets.) The leaflet thickness is set to a uniform value of 0.0386 cm.

Remark 6 The use of pinned rather than clamped boundary conditions is common in the structural analysis of BHVs reported previously [9,31,99–101]. However, the leaflets are, in fact, physically clamped at the attachment edge in most stented BHVs (see, e.g., [102,103]). As shown later in the paper, using clamped boundary conditions, the computed fully-open configuration of the leaflets is closer to the experimental measurements of pericardial BHV deformations [104–106] than results computed using pinned boundary conditions in [11,12].

To elucidate the physical significance of the Fung-type material model given by Eq. (15) in the context of BHV design, we compare its behavior to that of the classical St. Venant–Kirchhoff material, which assumes a linear

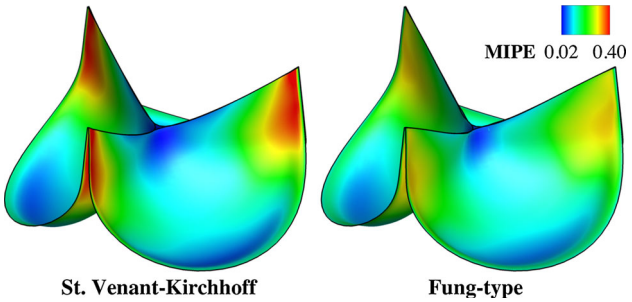

Fig. 5 Comparison between different isotropic material models. The valve is loaded with a spatially-uniform pressure of 100 mmHg. The maximum values of MIPE are 0.490 and 0.319 for St. Venant–Kirchhoff and Fung-type cases, respectively

stress–strain relationship and can not capture the exponential stiffening behavior of soft tissues. Fig. 5 compares MIPE[1] in pressure-loaded, fully-closed configurations of a valve modeled using the Fung-type material described above and a valve of the same geometry modeled using an isotropic St. Venant–Kirchhoff material with Young's modulus $E = 1.1 \times 10^7$ dyn/cm^2 and Poisson's ratio $\nu = 0.495$. The value of E is chosen such that the overall deformations are visually similar. The results show that the peak strain in the St. Venant–Kirchhoff material is much larger. The exponential term in the Fung-type energy functional ensures that regions of concentrated strain are energetically unfavorable, which has the effect of distributing strains more evenly through the leaflets.

3.2 Model of the artery and lumen

We model the artery as a 16 cm long elastic cylindrical tube with a three-lobed dilation near the BHV, as shown in Fig. 6. This dilation corresponds to the aortic sinus, which is known to play an important role in heart valve dynamics [107]. The cylindrical portion of the artery has an inside diameter of 2.6 cm and a wall thickness of 0.15 cm. The outflow boundary is 11 cm downstream of the valve, located at the right end of the channel, based on the orientation of Fig. 6. The inflow is located 5 cm upstream, at the left end of the channel. The designations of inflow and outflow are based on the prevailing flow direction during systole. In general, fluid may move in both directions and there is typically some regurgitation during diastole.

The arterial geometry is constructed using trivariate quadratic NURBS, allowing us to represent the circular portions exactly. We use a multi-patch design to avoid having a singularity at the center of the cylindrical sections (see Fig. 7). Basis functions are made C^0-continuous by repeated knot insertion at the fluid–solid interface, to capture the continuous but non-smooth velocity field across this jump in material type. The solid subdomain corresponds to the elastic aortic wall, while the fluid subdomain is the enclosed lumen. The mesh of the lumen and aortic wall consists of 102,960 and 12,480 elements, respectively. Mesh refinement is focused near the valve and sinus, as shown in Fig. 6. Figure 7 shows that the mesh is clustered toward the wall to better capture the boundary layer solution in those regions.

The arterial wall is modeled as a neo-Hookean material with dilatational penalty (see, e.g. [57,108]), where the shear and bulk modulii of the model are selected to produce a Young's modulus of 1.0×10^7 dyn/cm^2 and Poisson's ratio of 0.45 in the small-strain limit. The density of the arterial wall is 1.0 g/cm^3. Mass-proportional damping is added to model the interaction of the artery with surrounding tissue and interstitial fluid, with the damping coefficient set to 1.0×10^4 s^{-1}. The fluid density and viscosity in the lumen are set to $\rho_1 = 1.0$ g/cm^3 and $\mu = 3.0 \times 10^{-2}$ g/(cm s), respectively, which model the physical properties of human blood [109,110].

The inlet and outlet of the artery are free to slide in their cut planes, but constrained not to move in the orthogonal direction (see [42] for details). The outer wall of the artery has a zero-traction boundary condition. The BHV stent is surgically sutured to the aortic annulus at the suture ring. Since the stent is assumed not to move in this work, we apply homogeneous Dirichlet conditions to any control point of the solid portion of the artery mesh whose corresponding basis function's support intersects the stationary stent. Fig. 8 shows geometrically how the base ring intersects with the solid wall. The size of the ring can influence the potential space for blood flow and thus is important to be included in the FSI simulation. The stent also properly seals the gap in the fluid domain between the attached edges of the leaflets and the aortic wall.

3.3 Computations and results

This section sets up and compares the results of simulations of BHV function that are based on standalone structural dynamics and FSI.

3.3.1 Details of the structural dynamics simulation

In the structural dynamics computation, we model the transvalvular pressure (i.e., pressure difference between left ventricle and aorta) with the traction $-P(t)\mathbf{n}$, where $P(t)$ is the pressure difference at time t shown in Fig. 9, and $\mathbf{n}$ is the surface normal pointing from the aortic to the ventricular side of each leaflet. The transvalvular pressure signal is periodic with a period 0.86 s. As in the computations of [11,31], we use damping to model the viscous and inertial resistance of the surrounding fluid. We apply this damping as a traction $-c_d\mathbf{u}$, where $\mathbf{u}$ is the velocity of the shell midsurface and $c_d = 80$ g/(cm^2 s). This value of c_d ensures that the valve

[1] Maximum in-plane principal Green-Lagrange strain, the largest eigenvalue of $\mathbf{E}$.

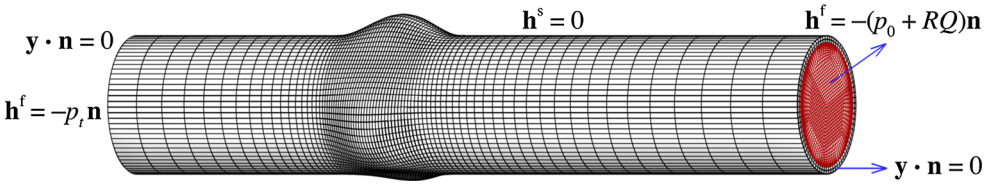

Fig. 6 A view of the arterial wall and lumen into which the valve is immersed

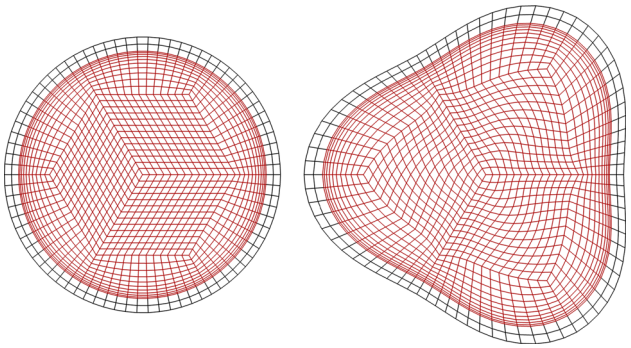

Fig. 7 Cross-sections of the fluid and solid meshes, taken from the cylindrical portion and the sinus

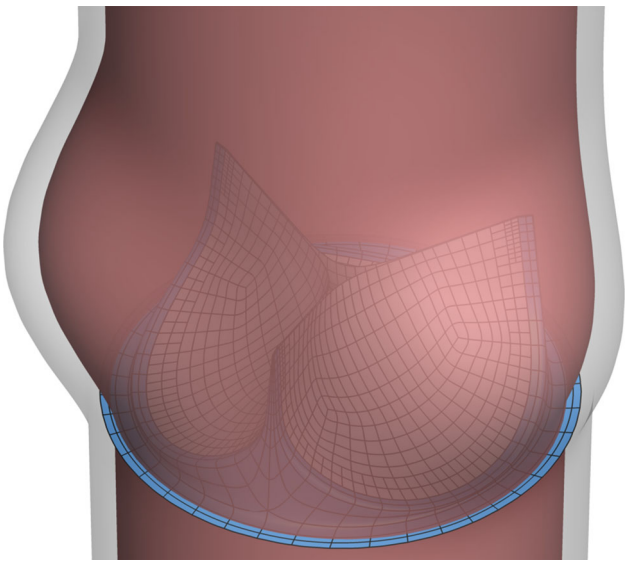

Fig. 8 The sinus, magnified and shown in relation to the valve leaflets and rigid stent. The suture ring of the stent intersects with the arterial wall

opens at a physiologically reasonable time scale when the given pressure is applied. The time step size for the dynamic simulation is $\Delta t = 1.0 \times 10^{-4}$ s.

3.3.2 Details of the FSI simulation

In the FSI simulation, we apply the physiologically-realistic left ventricular pressure time history from [111] (also plotted in Fig. 10) as a traction boundary condition at the inflow. The applied pressure signal is periodic with a period 0.86 s.

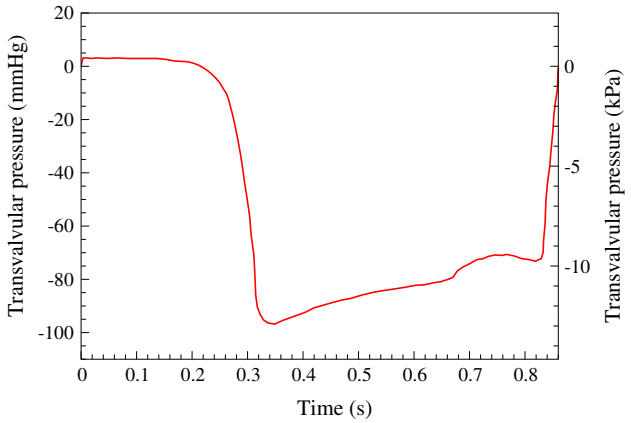

Fig. 9 Transvalvular pressure applied to the leaflets as a function of time. The profile is reproduced based on that reported in Kim et al. [31]. The original data has a cardiac cycle of 0.76 s. It is scaled to 0.86 s in our study to match the single cardiac cycle duration of our FSI simulation

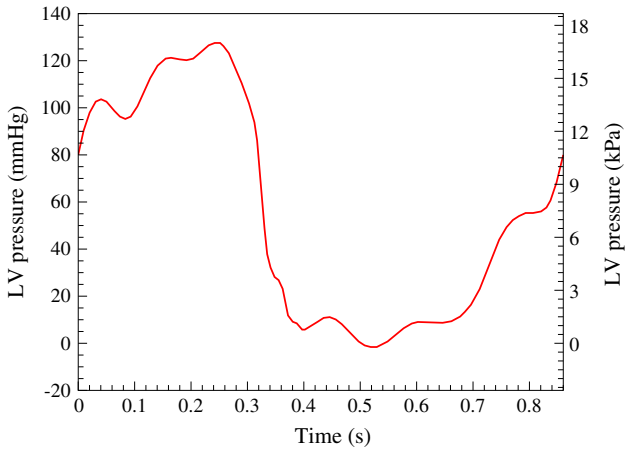

Fig. 10 Physiological left ventricular (LV) pressure profile applied at the inlet of the fluid domain. The duration of a single cardiac cycle is 0.86 s. The data is obtained from Yap et al. [111]

The traction $-(p_0+RQ)\mathbf{n}$ is applied at the outflow, where p_0 is a constant physiological pressure level, $\mathbf{n}$ is the outward-facing normal of the fluid domain, $R > 0$ is a resistance constant, and Q is the volumetric flow rate through the outflow. In the present computation, we set $p_0 = 80$ mmHg and $R = 70$ (dyn s)/cm^5. These values ensure a realistic transvalvular pressure difference of 80 mmHg across a closed valve, when $Q = 0$, while permitting a reasonable flow

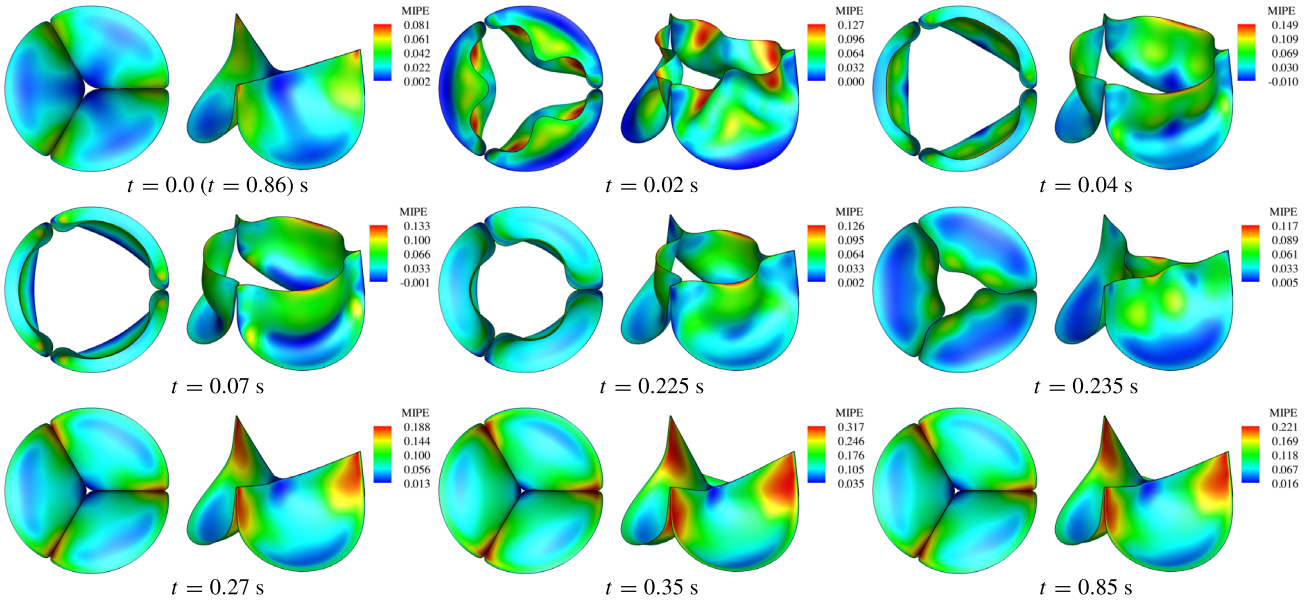

Fig. 11 Deformations of the valve from the structural dynamics computation, colored by the MIPE evaluated on the aortic side of the leaflet. Note the different scale for each time. The time t is synchronized with Fig. 9 for the current cycle

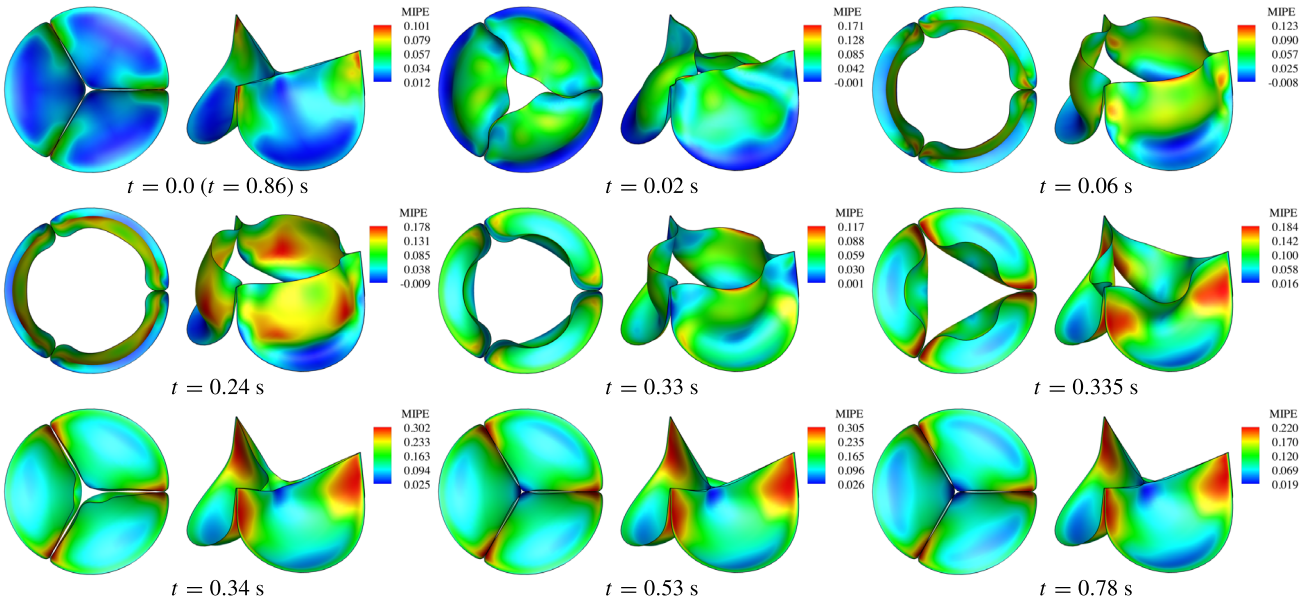

Fig. 12 Deformations of the valve from the FSI computation, colored by the MIPE evaluated on the aortic side of the leaflet. Note the different scale for each time. The time t is synchronized with Fig. 10 for the current cycle

rate during systole. We use backflow stabilization from [73], with $\beta = 0.5$, at both inlet and outlet surfaces. The normal and tangential velocity penalization parameters used in our FSI formulation are $\tau^B_{\mathrm{TAN}} = 2.0 \times 10^3$ g/(cm^2 s) and $\tau^B_{\mathrm{NOR}} = 2.0 \times 10^2$ g/(cm^2 s). As in our earlier studies [11,12], we set the τ_{M} scaling factor to $s^{\mathrm{shell}} = 10^6$ to obtain acceptable mass conservation near the immersed structure. As in the structural dynamics simulation, the time step size is $\Delta t = 1.0 \times 10^{-4}$ s. The stabilization parameter of the semi-implicit time integration scheme is $r = 10^{-5}$. This follows our recommendation from [35] to select $r \ll 1$.

Remark 7 As $r \to 0$, the semi-implicit time integration of the Lagrange multiplier field may be interpreted as a fully-implicit fluid–structure *displacement* penalization (cf. [11, Section 4.2.1]), with stiffness $\tau^B_{\mathrm{NOR}}/\Delta t = 2.0 \times 10^7$ dyn/cm^3. We may roughly estimate the physical significance of the time step splitting error incurred through semi-implicit integration by considering the fluid displace-

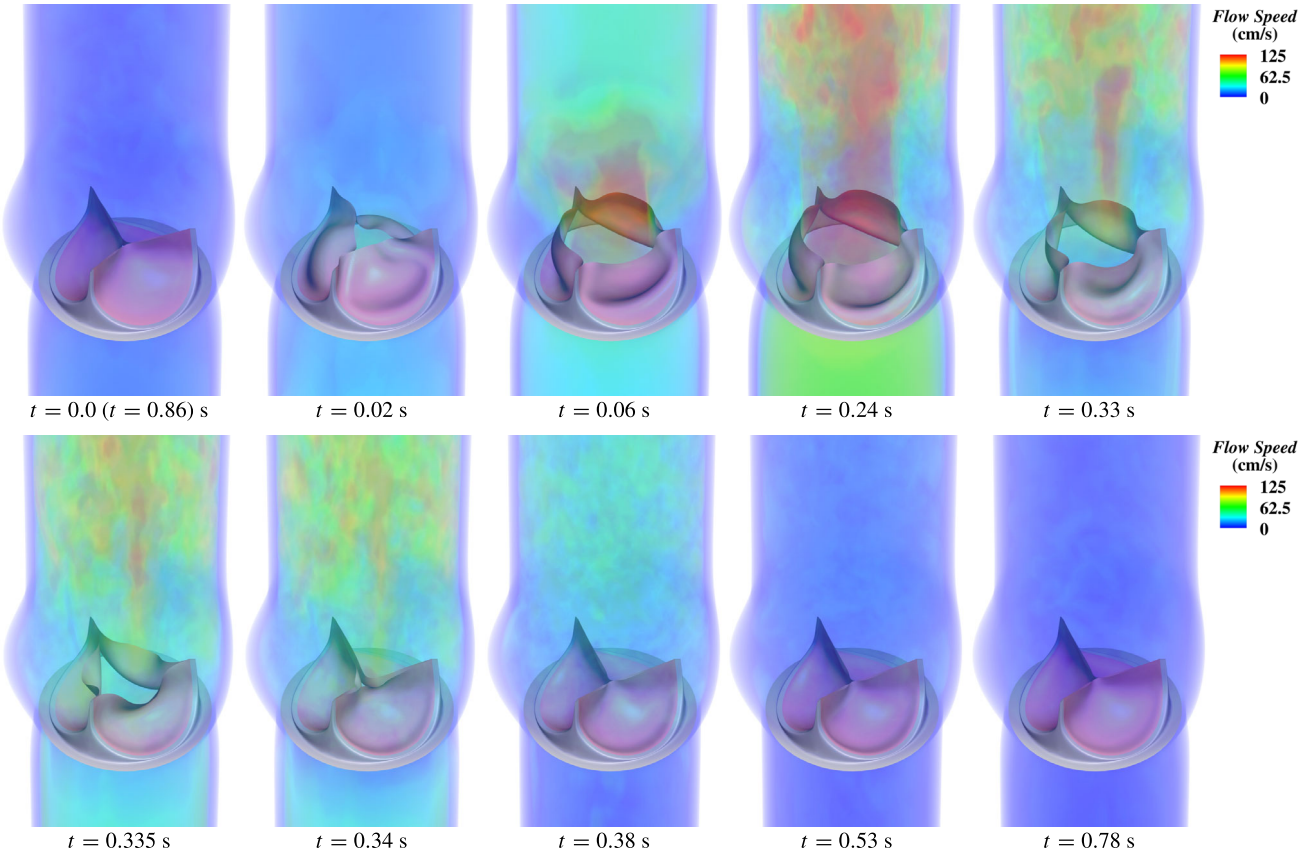

Fig. 13 Volume rendering of the velocity field at several points during a cardiac cycle. The time t is synchronized with Fig. 10 for the current cycle

ment through the valve in static equilibrium. The fluid would penetrate through the closed valve by a distance of only $\Delta P/(\tau_{\mathrm{NOR}}/\Delta t) = 0.005$ cm for diastolic pressure differences on the order of $\Delta P = 10^5$ dyn/cm^2. This is effectively within modeling error, considering that the penetration is nearly an order of magnitude smaller than the thickness of the leaflets.

3.3.3 Results and discussion

Figure 11 illustrates the deformations and strain distributions of the BHV model throughout a period of the prescribed pressure loading. Figure 12 shows the deformations and strains from a period of the FSI simulation, while Fig. 13 depicts the corresponding flow fields in the artery lumen. The volumetric flow rate through the top of the artery throughout the cardiac cycle is shown in Fig. 14.

Several important qualitative differences between the valve deformations in the dynamic and FSI computations are observed. Firstly, the opening process is very different. We can see from the snapshots at $t = 0.02$ s from Figs. 11 and 12 that the follower load in the dynamic computation drives the free edges of the leaflets apart immediately, while,

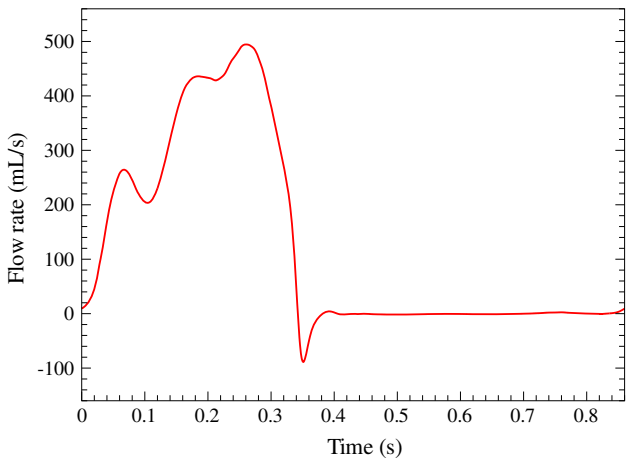

Fig. 14 Computed volumetric flow rate through the top of the fluid domain, during a full cardiac cycle of 0.86 s

in the FSI computation, the opening deformation initiates near the attached edge, then spreads toward the free edge. The opening of the leaflets in the FSI computation closely resembles the sequence of pericardial BHV leaflet deformations measured in vitro in [106], while the dynamic simulation

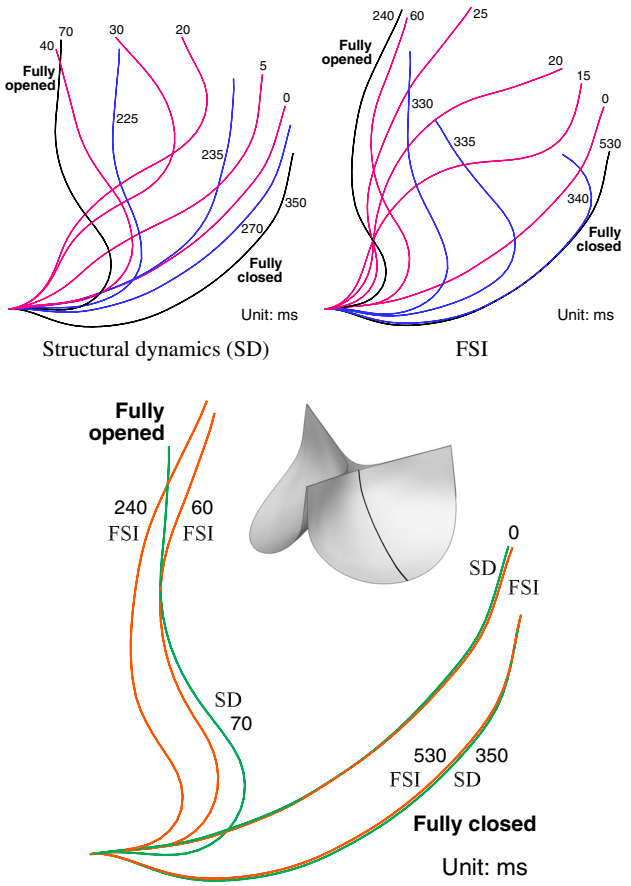

Fig. 15 Cross-sections of the time-dependent leaflet profile

exhibits unrealistic features. It is clear from the deformation cross-sections in Fig. 15 that a portion of the leaflet near the free edge ends up with the top (aortic) side of the leaflet facing downward. The follower load then pushes the free edge downward, exaggerating this feature. A similar artifact is apparent in the earlier dynamic computations of [31,101].

During the closing phase, the coaptation of the free edges of the leaflets is significantly delayed in the FSI computation; the free edges lean outward throughout the closing process, as is clear in Fig. 15. The follower load of the dynamic simulation drives the leaflets closed in a more uniform manner. This delayed closing of the free edge occurs in some pericardial bioprosthetic valve leaflets, and is evident in the photographic images taken and reported in [104]. This deformation is not observed in all valve leaflets, though (cf. [106]), and we therefore suspect that it is highly sensitive to valve geometry, leaflet material properties, and flow conditions. It seems unlikely that a uniform pressure follower load would cause this closing behavior, and it is not seen in any of the earlier structural dynamics computations of [9,31,101].

For the fully-closed configuration, the structural dynamics and FSI simulation results are quite similar, as can be seen in Fig. 15. Figure 13 shows that at this configuration, the flow is nearly hydrostatic. The BHV in the FSI computation is under hydrostatic pressure, which is at a similar level to the prescribed pressure load applied in the structural dynamics simulation. This result shows the applicability of the common modeling practice of approximating the influence of the fluid on the fully-closed valve as a pressure follower load, even though at other phases clear discrepancies were observed between dynamic and FSI computations.

4 Conclusions and further work

In this work we combine the geometry modeling and parametric design platform introduced in [19], thin shell constitutive modeling framework developed in [22], and immersogeometric FSI methodology proposed in [11,12] to perform high-fidelity BHV FSI with a greater level of automation, robustness and realism than achieved previously. We demonstrate the performance of our methods by applying them to a challenging problem of FSI analysis of BHVs at full scale and with full physiological realism. We illustrate the added value of including realistic material models of leaflet tissue and FSI coupling by comparing our results with those that omit material nonlinearity, or approximate the influence of the blood flow on the structure by means of applying prescribed uniform pressure loads and damping forces. The present effort represents the first step toward automated optimization of the leaflet design, to increase the useful life of BHVs.

Acknowledgments M.S. Sacks was supported by NIH/NHLBI Grant R01 HL108330. D. Kamensky was partially supported by the CSEM Graduate Fellowship. M.-C. Hsu, C. Wang and Y. Bazilevs were partially supported by the ARO Grant No. W911NF-14-1-0296. J. Kiendl and A. Reali were partially supported by the European Research Council through the FP7 Ideas Starting Grant No. 259229 ISOBIO. We thank the Texas Advanced Computing Center (TACC) at the University of Texas at Austin for providing HPC resources that have contributed to the research results reported in this paper.

References

1. Schoen FJ, Levy RJ (2005) Calcification of tissue heart valve substitutes: progress toward understanding and prevention. Ann Thorac Surg 79(3):1072–1080
2. Pibarot P, Dumesnil JG (2009) Prosthetic heart valves: selection of the optimal prosthesis and long-term management. Circulation 119(7):1034–1048
3. Li C-P, Chen S-F, Lo C-W, Lu P-C (2011) Turbulence characteristics downstream of a new trileaflet mechanical heart valve. ASAIO Journal 57(3):188–196
4. Yun BM, Wu J, Simon HA, Arjunon S, Sotiropoulos F, Aidun CK, Yoganathan AP (2012) A numerical investigation of blood damage in the hinge area of aortic bileaflet mechanical heart valves during the leakage phase. Ann Biomed Eng 40(7):1468–1485

5. Siddiqui RF, Abraham JR, Butany J (2009) Bioprosthetic heart valves: modes of failure. Histopathology 55:135–144
6. Sacks MS, Schoen FJ (2002) Collagen fiber disruption occurs independent of calcification in clinically explanted bioprosthetic heart valves. J Biomed Mater Res 62(3):359–371
7. Sacks MS, Mirnajafi A, Sun W, Schmidt P (2006) Bioprosthetic heart valve heterograft biomaterials: structure, mechanical behavior and computational simulation. Expert Rev Med Devices 3(6):817–834
8. Sun W, Abad A, Sacks MS (2005) Simulated bioprosthetic heart valve deformation under quasi-static loading. J Biomech Eng 127(6):905–914
9. Saleeb AF, Kumar A, Thomas VS (2013) The important roles of tissue anisotropy and tissue-to-tissue contact on the dynamical behavior of a symmetric tri-leaflet valve during multiple cardiac pressure cycles. Med Eng Phys 35(1):23–35
10. Auricchio F, Conti M, Ferrara A, Morganti S, Reali A (2014) Patient-specific simulation of a stentless aortic valve implant: the impact of fibres on leaflet performance. Comput Methods Biomech Biomed Eng 17(3):277–285
11. Kamensky D, Hsu M-C, Schillinger D, Evans JA, Aggarwal A, Bazilevs Y, Sacks MS, Hughes TJR (2015) An immersogeometric variational framework for fluid-structure interaction: application to bioprosthetic heart valves. Comput Methods Appl Mech Eng 284:1005–1053
12. Hsu M-C, Kamensky D, Bazilevs Y, Sacks MS, Hughes TJR (2014) Fluid-structure interaction analysis of bioprosthetic heart valves: significance of arterial wall deformation. Comput Mech 54:1055–1071
13. Peskin CS (1972) Flow patterns around heart valves: a numerical method. J Comput Phys 10(2):252–271
14. Peskin CS (2002) The immersed boundary method. Acta Numer 11:479–517
15. Mittal R, Iaccarino G (2005) Immersed boundary methods. Annu Rev Fluid Mech 37:239–261
16. Sotiropoulos F, Yang X (2014) Immersed boundary methods for simulating fluid-structure interaction. Prog Aerosp Sci 65: 1–21
17. Hughes TJR, Cottrell JA, Bazilevs Y (2005) Isogeometric analysis: CAD, finite elements, NURBS, exact geometry, and mesh refinement. Comput Methods Appl Mech Eng 194:4135–4195
18. Cottrell JA, Hughes TJR, Bazilevs Y (2009) Isogeometric analysis: toward integration of CAD and FEA. Wiley, Chichester
19. Hsu M-C, Wang C, Herrema AJ, Schillinger D, Ghoshal A, Bazilevs Y (2015) An interactive geometry modeling and parametric design platform for isogeometric analysis. Computers & Mathematics with Applications. doi:10.1016/j.camwa.2015.04.002
20. Kiendl J, Bletzinger K-U, Linhard J, Wüchner R (2009) Isogeometric shell analysis with Kirchhoff–Love elements. Comput Methods Appl Mech Eng 198:3902–3914
21. Kiendl J, Bazilevs Y, Hsu M-C, Wüchner R, Bletzinger K-U (2010) The bending strip method for isogeometric analysis of Kirchhoff–Love shell structures comprised of multiple patches. Comput Methods Appl Mech Eng 199:2403–2416
22. Kiendl J, Hsu M-C, Wu MCH, Reali A (2015) Isogeometric Kirchhoff-Love shell formulations for general hyperelastic materials. Computer Methods in Applied Mechanics and Engineering. doi:10.1016/j.cma.2015.03.010
23. Rhinoceros (2015). http://www.rhino3d.com/
24. Autodesk T-Splines Plug-in for Rhino (2015). http://www.tsplines.com/products/tsplines-for-rhino.html
25. Piegl L, Tiller W (1997) The NURBS Book (Monographs in Visual Communication), 2nd edn. Springer, New York
26. Scott MA, Hughes TJR, Sederberg TW, Sederberg MT (2014) An integrated approach to engineering design and analysis using the Autodesk T-spline plugin for Rhino3d. ICES REPORT 14–33, The Institute for Computational Engineering and Sciences, The University of Texas at Austin, Sept 2014
27. Li X, Zheng J, Sederberg TW, Hughes TJR, Scott MA (2012) On linear independence of T-spline blending functions. Comput Aided Geom Des 29(1):63–76
28. Li X, Scott MA (2014) Analysis-suitable T-splines: Characterization, refineability, and approximation. Mathematical Models and Methods in Applied Sciences 24:1141–1164
29. Grasshopper (2015). http://www.grasshopper3d.com/
30. Rhino Developer Tools (2015). http://wiki.mcneel.com/developer/home
31. Kim H, Lu J, Sacks MS, Chandran KB (2008) Dynamic simulation of bioprosthetic heart valves using a stress resultant shell model. Ann Biomed Eng 36(2):262–275
32. Sederberg TW, Cardon DL, Finnigan GT, North NS, Zheng J, Lyche T (2004) T-spline simplification and local refinement. ACM Trans Graph 23(3):276–283
33. Holzapfel GA (2000) Nonlinear solid mechanics: a continuum approach for engineering. Wiley, Chichester
34. Scott MA, Borden MJ, Verhoosel CV, Sederberg TW, Hughes TJR (2011) Isogeometric finite element data structures based on Bézier extraction of T-splines. Int J Numer Methods Eng 88:126–156
35. Kamensky D, Evans JA, Hsu M-C (2015) Stability and conservation properties of collocated constraints in immersogeometric fluid-thin structure interaction analysis. *Communications in Computational Physics*. Accepted
36. Hughes TJR, Liu WK, Zimmermann TK (1981) Lagrangian-Eulerian finite element formulation for incompressible viscous flows. Comput Methods Appl Mech Eng 29:329–349
37. Donea J, Giuliani S, Halleux JP (1982) An arbitrary Lagrangian-Eulerian finite element method for transient dynamic fluid-structure interactions. Comput Methods Appl Mech Eng 33(1–3):689–723
38. Formaggia L, Gerbeau JF, Nobile F, Quarteroni A (2001) On the coupling of 3D and 1D Navier-Stokes equations for flow problems in compliant vessels. Comput Methods Appl Mech Eng 191:561–582
39. Gerbeau J-F, Vidrascu M, Frey P (2005) Fluid-structure interaction in blood flows on geometries based on medical imaging. Comput Struct 83:155–165
40. Nobile F, Vergara C (2008) An effective fluid-structure interaction formulation for vascular dynamics by generalized Robin conditions. SIAM J Sci Comput 30:731–763
41. Bazilevs Y, Hsu M-C, Zhang Y, Wang W, Liang X, Kvamsdal T, Brekken R, Isaksen J (2010) A fully-coupled fluid-structure interaction simulation of cerebral aneurysms. Comput Mech 46:3–16
42. Bazilevs Y, Hsu M-C, Zhang Y, Wang W, Kvamsdal T, Hentschel S, Isaksen J (2010) Computational fluid-structure interaction: methods and application to cerebral aneurysms. Biomech Model Mechanobiol 9:481–498
43. Perego M, Veneziani A, Vergara C (2011) A variational approach for estimating the compliance of the cardiovascular tissue: an inverse fluid-structure interaction problem. SIAM J Sci Comput 33:1181–1211
44. Hsu M-C, Bazilevs Y (2011) Blood vessel tissue prestress modeling for vascular fluid-structure interaction simulations. Finite Elem Anal Des 47:593–599
45. Takizawa K, Bazilevs Y, Tezduyar TE (2012) Space-time and ALE-VMS techniques for patient-specific cardiovascular fluid-structure interaction modeling. Arch Comput Methods Eng 19:171–225
46. Takizawa K, Bazilevs Y, Tezduyar TE, Long CC, Marsden AL, Schjodt K (2014) ST and ALE-VMS methods for patient-specific cardiovascular fluid mechanics modeling. Math Models Methods Appl Sci 24:2437–2486

47. Tezduyar TE (1992) Stabilized finite element formulations for incompressible flow computations. Adv Appl Mech 28:1–44
48. Tezduyar TE (2003) Computation of moving boundaries and interfaces and stabilization parameters. Int J Numer Methods Fluids 43:555–575
49. Tezduyar TE, Sathe S (2007) Modelling of fluid-structure interactions with the space-time finite elements: solution techniques. Int J Numer Methods Fluids 54(6–8):855–900
50. Takizawa K, Tezduyar TE (2011) Multiscale space-time fluid-structure interaction techniques. Comput Mech 48:247–267
51. Takizawa K, Tezduyar TE (2012) Space-time fluid-structure interaction methods. Math Models Methods Appl Sci 22:1230001
52. Takizawa K, Schjodt K, Puntel A, Kostov N, Tezduyar TE (2013) Patient-specific computational analysis of the influence of a stent on the unsteady flow in cerebral aneurysms. Comput Mech 51:1061–1073
53. Takizawa K, Tezduyar TE, Buscher A, Asada S (2014) Space-time interface-tracking with topology change (ST-TC). Comput Mech 54:955–971
54. Takizawa K, Torii R, Takagi H, Tezduyar TE, Xu XY (2014) Coronary arterial dynamics computation with medical-image-based time-dependent anatomical models and element-based zero-stress state estimates. Comput Mech 54:1047–1053
55. Takizawa K, Tezduyar TE, Buscher A, Asada S (2014) Space-time fluid mechanics computation of heart valve models. Comput Mech 54:973–986
56. Bazilevs Y, Calo VM, Zhang Y, Hughes TJR (2006) Isogeometric fluid-structure interaction analysis with applications to arterial blood flow. Comput Mech 38:310–322
57. Bazilevs Y, Calo VM, Hughes TJR, Zhang Y (2008) Isogeometric fluid-structure interaction: theory, algorithms, and computations. Comput Mech 43:3–37
58. Bazilevs Y, Hsu M-C, Takizawa K, Tezduyar TE (2012) ALE-VMS and ST-VMS methods for computer modeling of wind-turbine rotor aerodynamics and fluid-structure interaction. Math Models Methods Appl Sci 22:1230002
59. Takizawa K, Bazilevs Y, Tezduyar TE, Hsu M-C, Øiseth O, Mathisen KM, Kostov N, McIntyre S (2014) Engineering analysis and design with ALE-VMS and Space-Time methods. Arch Comput Methods Eng 21:481–508
60. Bazilevs Y, Takizawa K, Tezduyar TE, Hsu M-C, Kostov N, McIntyre S (2014) Aerodynamic and FSI analysis of wind turbines with the ALE-VMS and ST-VMS methods. Arch Comput Methods Eng 21:359–398
61. Brooks AN, Hughes TJR (1982) Streamline upwind/Petrov-Galerkin formulations for convection dominated flows with particular emphasis on the incompressible Navier-Stokes equations. Comput Methods Appl Mech Eng 32:199–259
62. Tezduyar TE, Osawa Y (2000) Finite element stabilization parameters computed from element matrices and vectors. Comput Methods Appl Mech Eng 190:411–430
63. Hughes TJR, Mazzei L, Jansen KE (2000) Large eddy simulation and the variational multiscale method. Comput Vis Sci 3:47–59
64. Hughes TJR, Mazzei L, Oberai AA, Wray A (2001) The multiscale formulation of large eddy simulation: Decay of homogeneous isotropic turbulence. Phys Fluids 13:505–512
65. Hughes TJR, Scovazzi G, Franca LP (2004) Multiscale and stabilized methods. In: Stein E, de Borst R, Hughes TJR (eds) Encyclopedia of computational mechanics, Vol. 3: Fluids, chap. 2. Wiley, Hoboken
66. Bazilevs Y, Calo VM, Cottrel JA, Hughes TJR, Reali A, Scovazzi G (2007) Variational multiscale residual-based turbulence modeling for large eddy simulation of incompressible flows. Comput Methods Appl Mech Eng 197:173–201
67. Hsu M-C, Bazilevs Y, Calo VM, Tezduyar TE, Hughes TJR (2010) Improving stability of stabilized and multiscale formulations in flow simulations at small time steps. Comput Methods Appl Mech Eng 199:828–840
68. Bazilevs Y, Hsu M-C, Scott MA (2012) Isogeometric fluid-structure interaction analysis with emphasis on non-matching discretizations, and with application to wind turbines. Comput Methods Appl Mech Eng 249–252:28–41
69. Wriggers P (2006) Comput Contact Mech, 2nd edn. Springer, Berlin Heidelberg
70. Laursen TA (2003) Computational contact and impact mechanics: fundamentals of modeling interfacial phenomena in nonlinear finite element analysis. Springer, Berlin Heidelberg
71. Morganti S, Auricchio F, Benson DJ, Gambarin FI, Hartmann S, Hughes TJR, Reali A (2015) Patient-specific isogeometric structural analysis of aortic valve closure. Comput Methods Appl Mech Eng 284:508–520
72. Bazilevs Y, Gohean JR, Hughes TJR, Moser RD, Zhang Y (2009) Patient-specific isogeometric fluid-structure interaction analysis of thoracic aortic blood flow due to implantation of the Jarvik 2000 left ventricular assist device. Comput Methods Appl Mech Eng 198:3534–3550
73. Esmaily-Moghadam M, Bazilevs Y, Hsia T-Y, Vignon-Clementel IE, MOCHA (2011) A comparison of outlet boundary treatments for prevention of backflow divergence with relevance to blood flow simulations. Comput Mech 48:277–291
74. Chung J, Hulbert GM (1993) A time integration algorithm for structural dynamics with improved numerical dissipation: the generalized-α method. J Appl Mech 60:371–375
75. Jansen KE, Whiting CH, Hulbert GM (2000) A generalized-α method for integrating the filtered Navier-Stokes equations with a stabilized finite element method. Comput Methods Appl Mech Eng 190:305–319
76. Tezduyar TE, Sathe S, Stein K (2006) Solution techniques for the fully-discretized equations in computation of fluid-structure interactions with the space-time formulations. Comput Methods Appl Mech Eng 195:5743–5753
77. Tezduyar TE, Sathe S, Keedy R, Stein K (2006) Space-time finite element techniques for computation of fluid-structure interactions. Comput Methods Appl Mech Eng 195:2002–2027
78. Tezduyar TE, Sathe S (2007) Modeling of fluid-structure interactions with the space-time finite elements: solution techniques. Int J Numer Methods Fluids 54:855–900
79. Bazilevs Y, Takizawa K, Tezduyar TE (2013) Computational fluid-structure interaction: methods and applications. Wiley, Chichester
80. Tezduyar TE, Takizawa K, Moorman C, Wright S, Christopher J (2010) Space-time finite element computation of complex fluid-structure interactions. Int J Numer Methods Fluids 64:1201–1218
81. Tezduyar TE (2001) Finite element methods for flow problems with moving boundaries and interfaces. Arch Comput Methods Eng 8:83–130
82. Akin JE, Tezduyar TE, Ungor M (2007) Computation of flow problems with the mixed interface-tracking/interface-capturing technique (MITICT). Comput Fluids 36:2–11
83. Cruchaga MA, Celentano DJ, Tezduyar TE (2007) A numerical model based on the mixed interface-tracking/interface-capturing technique (MITICT) for flows with fluid-solid and fluid-fluid interfaces. Int J Numer Methods Fluids 54:1021–1030
84. Akkerman I, Bazilevs Y, Benson DJ, Farthing MW, Kees CE (2011) Free-surface flow and fluid-object interaction modeling with emphasis on ship hydrodynamics. Journal of Applied Mechanics, accepted for publication

85. Wick T (2014) Flapping and contact FSI computations with the fluid-solid interface-tracking/interface-capturing technique and mesh adaptivity. Comput Mech 53(1):29–43
86. Tezduyar T, Aliabadi S, Behr M, Johnson A, Mittal S (1993) Parallel finite-element computation of 3D flows. Computer 26(10): 27–36
87. Johnson AA, Tezduyar TE (1994) Mesh update strategies in parallel finite element computations of flow problems with moving boundaries and interfaces. Comput Methods Appl Mech Eng 119:73–94
88. Stein K, Tezduyar T, Benney R (2003) Mesh moving techniques for fluid-structure interactions with large displacements. J Appl Mech 70:58–63
89. Stein K, Tezduyar TE, Benney R (2004) Automatic mesh update with the solid-extension mesh moving technique. Comput Methods Appl Mech Eng 193:2019–2032
90. Bazilevs Y, Hughes TJR (2007) Weak imposition of Dirichlet boundary conditions in fluid mechanics. Comput Fluids 36: 12–26
91. Bazilevs Y, Michler C, Calo VM, Hughes TJR (2007) Weak Dirichlet boundary conditions for wall-bounded turbulent flows. Comput Methods Appl Mech Eng 196:4853–4862
92. Bazilevs Y, Michler C, Calo VM, Hughes TJR (2010) Isogeometric variational multiscale modeling of wall-bounded turbulent flows with weakly enforced boundary conditions on unstretched meshes. Comput Methods Appl Mech Eng 199:780–790
93. Hsu M-C, Akkerman I, Bazilevs Y (2012) Wind turbine aerodynamics using ALE-VMS: validation and the role of weakly enforced boundary conditions. Comput Mech 50:499–511
94. Tong P, Fung Y-C (1976) The stress-strain relationship for the skin. J Biomech 9(10):649–657
95. Fung YC (1993) Biomechanics: mechanical properties of living tissues, 2nd edn. Springer, New York
96. Sun W, Sacks MS, Sellaro TL, Slaughter WS, Scott MJ (2003) Biaxial mechanical response of bioprosthetic heart valve biomaterials to high in-plane shear. J Biomech Eng 125(3):372–380
97. Fan R, Sacks MS (2014) Simulation of planar soft tissues using a structural constitutive model: finite element implementation and validation. J Biomech 47(9):2043–2054
98. Mirnajafi A, Raymer J, Scott MJ, Sacks MS (2005) The effects of collagen fiber orientation on the flexural properties of pericardial heterograft biomaterials. Biomaterials 26(7):795–804
99. Kim H, Chandran KB, Sacks MS, Lu J (2007) An experimentally derived stress resultant shell model for heart valve dynamic simulations. Ann Biomed Eng 35(1):30–44
100. Li K, Sun W (2010) Simulated thin pericardial bioprosthetic valve leaflet deformation under static pressure-only loading conditions: implications for percutaneous valves. Ann Biomed Eng 38(8):2690–2701
101. Burriesci G, Howard IC, Patterson EA (1999) Influence of anisotropy on the mechanical behaviour of bioprosthetic heart valves. J Med Eng Technol 23(6):203–215
102. Huynh VL, Nguyen T, Lam HL, Guo XG, Kafesjian R (2003) Cloth-covered stents for tissue heart valves, US Patent 6,585,766
103. Piazza N, Bleiziffer S, Brockmann G, Hendrick R, Deutsch MA, Opitz A, Mazzitelli D, Tassani-Prell P, Schreiber C, Lange R (2011) Transcatheter aortic valve implantation for failing surgical aortic bioprosthetic valve. JACC 4(7):721–732
104. Gao ZB, Pandya S, Hosein N, Sacks MS, Hwang NHC (2000) Bioprosthetic heart valve leaflet motion monitored by dual camera stereo photogrammetry. J Biomech 33(2):199–207
105. Gao BZ, Pandya S, Arana C, Hwang NHC (2002) Bioprosthetic heart valve leaflet deformation monitored by double-pulse stereo photogrammetry. Ann Biomed Eng 30(1):11–18
106. Iyengar AKS, Sugimoto H, Smith DB, Sacks MS (2001) Dynamic in vitro quantification of bioprosthetic heart valve leaflet motion using structured light projection. Ann Biomed Eng 29(11): 963–973
107. Bellhouse BJ, Bellhouse FH (1968) Mechanism of closure of the aortic valve. Nature 217(5123):86–87
108. Simo JC, Hughes TJR (1998) Computational inelasticity. Springer, New York
109. Kenner T (1989) The measurement of blood density and its meaning. Basic Res Cardiol 84(2):111–124
110. Rosencranz R, Bogen SA (2006) Clinical laboratory measurement of serum, plasma, and blood viscosity. Am J Clin Pathol 125: S78–S86
111. Yap CH, Saikrishnan N, Tamilselvan G, Yoganathan AP (2011) Experimental technique of measuring dynamic fluid shear stress on the aortic surface of the aortic valve leaflet. J Biomech Eng 133(6):061007